PROCEEDINGS, Thirty-Seventh Workshop on Geothermal Reservoir Engineering
Stanford University, Stanford, California, January 30 - February 1, 2012
SGP-TR-194

BOREHOLE PRECONDITIONING OF GEOTHERMAL WELLS FOR ENHANCED GEOTHERMAL SYSTEM RESERVOIR DEVELOPMENT

A. Diek[1], L. White[1], J.-C. Roegiers[1], J. Moore[2] & J. D. McLennan[2]

[1]The University of Oklahoma
100 E. Boyd St., Norman, OK 73019, USA
[2]Energy & Geoscience Institute, University of Utah, Salt Lake City, UT 84108, USA
e-mail: jroegiers@ou.edu

ABSTRACT

Thermal stimulation can be utilized to precondition a well to optimize fracturing and production during Enhanced Geothermal System (EGS) reservoir development. A finite element model was developed for the fully coupled processes consisting of: thermoporoelastic deformation, hydraulic conduction, thermal osmosis, heat conduction, pressure thermal effect, and the interconvertibility of mechanical and thermal energy. The model has been applied to Raft River geothermal well RRG-9, which will be subjected to thermal and hydraulic stimulation as part of a Department of Energy EGS demonstration project. RRG-9 encountered a temperature of ~140^{o}C.

The two-dimensional fully coupled model assumes that the material diffusion coefficient for the pressure is spatially dependent. Thus, the model can simulate the effect of healed fractures around a borehole subjected to non-hydrostatic in situ stress fields. In this study, the effects of cooling RRG-9 by 60, 40 and 20^{o}C are evaluated

The results indicate that cooling induces a decrease in the pore pressure around the borehole. In addition to ΔT, it was found that the time (t), the borehole pressure (p_B), and the angle (θ) around the borehole perimeter influence the stresses around the borehole. For example, (1) lower borehole temperature, or (2) lower borehole pressure, or (3) a shorter time, results in higher (more compressive or less tensile) effective radial stresses and lower (less compressive or more tensile) effective tangential stresses around the wellbore. For this case of RRG-9, the maximum tensile (most negative value) effective tangential stress occurs at the borehole wall while the maximum tensile effective radial stress occurs within the formation. The tensile effective tangential stress could start the fracture at the borehole wall while the tensile effective radial stress could cause time-delayed spalling. Note that compression is assumed positive and tension negative.

INTRODUCTION

The Raft River geothermal system is located in southern Idaho within the Raft River Valley (Fig. 1). The field, which is owned and operated by U.S. Geothermal Inc., has been selected as an Enhanced Geothermal System (EGS) demonstration site by the U. S. Department of Energy's Geothermal Technologies Program. The geothermal resource at Raft River was discovered sometime prior to 1950 when two shallow agricultural wells, the Bridge and Crank wells, encountered boiling water. Since its discovery, nine deep wells (> 1500 m depth) with bottom hole temperatures ranging from 133 to 149^{o}C, have been drilled (Fig. 1). Four of these currently provide geothermal water to the field's 13 MW net capacity power plant. Three others are used for reinjection. The plant has been in operation since 2008.

The Raft River reservoir is developed in fractured Proterozoic schist and quartzite, and Archean quartz monzonite. During mid-Tertiary time, the basement complex was deformed and covered by approximately 1500 m of late Tertiary sedimentary and volcanic deposits. Three major fault zones have been identified in the vicinity of the well field (Fig. 1). These faults offset the Tertiary and Quaternary deposits but do not significantly displace the Tertiary-Proterozoic contact within the well field. The Bridge and the Horse Wells Fault Zones, on the west side of the valley, trend north to northeast and are inferred to be listric in nature, flattening at the basement-sediment contact (Covington, 1980). These fault zones appear to terminate southward at a poorly understood but hydraulically important feature referred to as the Narrows Structure. This structure is interpreted to be a right lateral strike slip basement shear (Mabey et al., 1978). Waters sampled from the southeastern wells (wells RRG-3, 6, 7 and 11) are enriched in Cl (2000-4000 mg/l) compared to waters sampled from the northeastern wells (wells RRG-1, 2 and 5; Cl ~1000 mg/l) (Ayling et al., 2011). They suggested the Narrows Structure acts as a low

permeability boundary separating the two groups of geothermal waters. Reactivation of the Narrows Structure may account for the easterly trending Quaternary faults south of the well field.

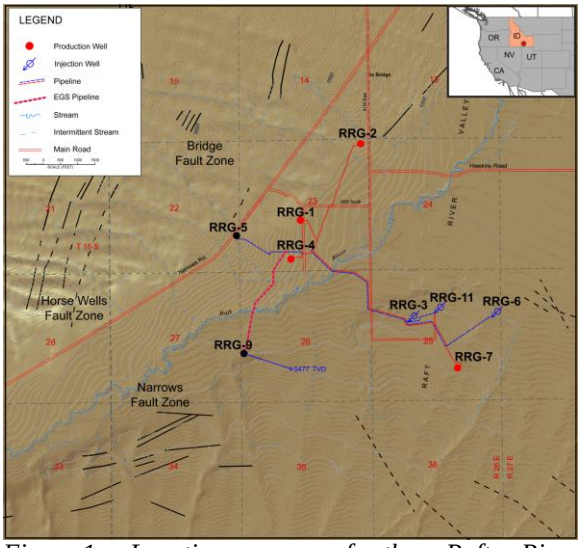

Figure 1: Location map of the Raft River geothermal field showing injection and production wells and Quaternary faults. For clarity, only the bottom hole location of RRG-9, the stimulation well, is shown.

Well RRG-9 is the target stimulation well for the EGS program. It was drilled southwest of the main well field to 1855.9 m MD (6089 ft MD). The well is deviated to the southeast and penetrated the Proterozoic reservoir rocks at a depth of 1611.2 m MD (5286 ft MD). A maximum temperature of 139°C was encountered at TD. The demonstration project has two major objectives. The first is to develop and demonstrate techniques required to form and sustain EGS reservoirs. The second is to improve the performance and output of the Raft River geothermal field by increasing production or injectivity.

This project brings a novel approach to geothermal reservoir stimulation. A series of staged stimulation treatments will be conducted in order to assess mechanisms for increasing the fractured reservoir volume. The reservoir will be first pre-conditioned by thermal fracturing using low-temperature water injection. There is considerable evidence from geothermal field operations worldwide, including those at Raft River, and numerous examples from the petroleum literature, indicating that injection of cool water can significantly enhance injectivity. This increase is attributed to fracturing caused by thermal stresses generated within the cooling rock mass. It can be anticipated that some of these dominantly tensile thermal fractures will intersect preexisting zones of weakness. These zones may also fail during the stimulation via shear from effective stress changes. Thus it may be possible to access a larger volume of the target region by taking advantage of the thermoelastic stress alteration – either on its own or in conjunction with subsequent hydraulic injection. A high rate, large volume conventional stimulation will follow the thermal treatments. Microseismic activity and pressure transient evaluations will be used to monitor the effects of each stimulation stage on the fracture volume and interconnectivity.

A FULLY COUPLED THERMOPOROELASTIC MODEL

General

A general theory of thermoporoelasticity has been developed that fully couples mechanical, hydraulic, and thermal processes in fluid-saturated rock (Diek et al., 2011). The theory satisfies the first and second laws of thermodynamics and is based on concepts of irreversible thermodynamics, a novel rock constitutive relation, and Onsager's transport phenomenology. Field equations were developed in terms of five independent variables, namely the three solid displacements, u_i, the pore pressure, p, and the absolute temperature, T. These equations are obtained by implementing the rock constitutive and transport equations into the momentum, fluid mass, and energy balance equations. The rock constitutive equations are derived from a state function that describes the manner in which the potential energy of the rock changes with respect to time. The temporal evolution of the potential energy is obtained by combining the localized internal energy and entropy balance equations which satisfy the first and second law of thermodynamics, respectively. The rock constitutive equations describe the response of the rock to mechanical and thermal loading. They express the temporal evolution of the total stresses, the variation of the fluid content, and the rock entropy in terms of the forgoing five independent variables. The transport relationships that couple the influx and efflux of fluid and heat to their driving forces are derived from the definition of the internal entropy production rate and its associated generalized forces. The temperature is locally equilibrated between the fluid and the solid.

Rock Constitutive Equations

In the case of complete isotropy, linear responses of the total stresses $\sigma_{ij,}$ variation of the fluid content ζ, and the rock entropy S (per referential volume) to the strain components ε_{ij}, pore pressure p, and absolute temperature T are as follows:

$$\sigma_{ij} = 2G\varepsilon_{ij} + \left(K - \frac{2G}{3}\right)\varepsilon_{kk}\delta_{ij} - \alpha p\delta_{ij} - AT\delta_{ij} \qquad (1)$$

$$\dot{\zeta} = \alpha\dot{\varepsilon} + \Psi\dot{p} + \Gamma\dot{T} \qquad (2)$$

$$\dot{S} = \dot{S}_s + \phi\rho_f \dot{s}_f = A\dot{\varepsilon}_{ii} + \Gamma\dot{p} + \Lambda\dot{T} \tag{3}$$

where S_s is the solid entropy per referential volume, ϕ is the reference porosity, and ρ_f and s_f are the fluid density and specific entropy, respectively. The coefficients in the constitutive equations (1), (2), and (3) are:

$$\alpha = \left(1 - \frac{K}{K_s}\right), \quad \psi = \left(\frac{\alpha - \phi}{K_s}\right), \quad A = K\beta_s, \tag{4}$$

$$\Xi = (\alpha - \phi)\beta_s, \; \Gamma = (\Xi - \phi\beta_f), \; \Psi = \left(\psi + \frac{\phi}{K_f}\right), \tag{5}$$

$$\Lambda = \frac{C}{T_F}, \quad C = (1-\phi)\rho_s C_s + \phi\rho_f C_f \tag{6}$$

where α is Biot's effective stress coefficient, and K and G denote the rock's bulk and shear moduli, respectively. K_s denotes the solid bulk modulus, β_s represents the solid volumetric thermal expansion coefficient, ρ_s denotes the solid mass density, C_s is the solid specific heat, K_f denotes the fluid bulk modulus, β_f represents the fluid volumetric thermal expansion coefficient, C_f denote the fluid specific heat capacity, and T_F is the reference formation temperature.

Transport Equations

In the presence of hydraulic and thermal gradients the fluid mass flux, J_f, and the heat flux, J_q, can be related to the driving forces through experimentally measurable phenomenological coefficients:

$$\dot{w} = \frac{J_f}{\rho_f} = -\frac{k}{\eta}\nabla p + K^T \nabla T \tag{7}$$

$$J_q = T_F K^T \nabla p - k^T \nabla T \tag{8}$$

where $\dot{w}$ is Darcy's filter velocity, and Onsager's reciprocity theorem is assumed (Onsager, 1931). The fluid mass flux is due to the coupling of two processes: hydraulic conduction and thermal osmosis. The heat flux is due to the coupling of the pressure thermal effect and heat conduction. The constants are defined as follows: k is the intrinsic permeability, η is the viscosity of the fluid, K^T is the thermal osmosis coefficient, and k^T is the rock thermal conductivity coefficient, defined as:

$$k^T = (1-\phi)\rho_s k_s^T + \phi\rho_f k_f^T \tag{9}$$

where $k^T{}_s$ and $k^T{}_f$ are the thermal conductivity coefficients of the solid matrix and fluid, respectively.

Field Equations

Field equations were developed by substituting the rock constitutive and transport equations into the momentum, mass, and energy balance equations, respectively:

$$\sigma_{ij,j} = 0 \tag{10}$$

$$\dot{\zeta} + (\nabla \cdot \dot{w}) = 0 \tag{11}$$

$$T_F \dot{S} + (\nabla \cdot J_q) = 0 \tag{12}$$

Navier-type Equations

The three fully coupled Navier-type field equations are obtained by substituting the constitutive equations (1) into the momentum balance equation in Eq. (10):

$$\left(K + \frac{G}{3}\right)\nabla(\nabla \cdot u) + G\nabla^2 u - \alpha\nabla p - A\nabla T = 0 \tag{13}$$

Fluid Diffusion Equation

The fully coupled fluid diffusion equation is obtained by substituting the constitutive equation (2) and flux (7) into the linearized fluid mass balance in Eq. (11):

$$\alpha(\nabla \cdot \dot{u}) + \Psi\dot{p} + \Gamma\dot{T} - (k/\eta)\nabla^2 p + K^T \nabla^2 T = 0 \tag{14}$$

Thermal Diffusion Equation

The fully coupled thermal diffusion equation is obtained by substituting the constitutive equation (3) and flux (8) into the linearized energy balance in Eq. (12):

$$A(\nabla \cdot \dot{u}) + \Gamma\dot{p} + \Lambda\dot{T} + K^T \nabla^2 p - k^T\left(\frac{\nabla^2 T}{T_F}\right) = 0 \tag{15}$$

MATHEMATICAL ANALYSIS

The approach used in this study was to formulate the diffusion system in divergence form with a spatially dependent diffusion matrix. The specific form of the matrix depends on what diffusion effect is desired to be captured. The weak form of the diffusion system is then obtained to allow for discontinuous behavior in the diffusion properties. The elastic model is assumed to be isotropic with constant coefficients.

The pore pressure, p, and temperature, T, satisfy a system (PT) of coupled partial differential equations determining an initial boundary value problem defined in an annular region Ω exterior to the borehole. Although this region is infinite, it is specified with an inner radius, R_B, and a finite far-field radius, R_F. The PT system is then coupled with an elastic Navier-type equation determining displacements, u, and stresses, σ_{rr}, and $\sigma_{\theta\theta}$, in the

region around the borehole. The time-derivative of the displacement vector satisfies Navier-type equations (13) in Ω x (0, t_f). Typically, the displacement **u** is expressed in terms of polar coordinates as:

$$\mathbf{u}(r, \theta) = u(r, \theta)\mathbf{i}_r + v(r, \theta)\, \mathbf{i}_\theta \quad (16)$$

Boundary conditions are specified using borehole conditions that the radial stress satisfy

$$\sigma_{rr} = p_B \quad (17)$$

so that at the borehole boundary radial stress equals the borehole pressure. In the far-field, radial and tangential stresses are the formation stresses so that

$$\sigma_{rr} = \frac{(S_{xx} + S_{yy})}{2} + S_{xy} \sin 2\theta + \frac{(S_{xx} - S_{yy})\cos 2\theta}{2} \quad (18)$$

$$\sigma_{\theta\theta} = \frac{(S_{xx} + S_{yy})}{2} - S_{xy} \sin 2\theta - \frac{(S_{xx} - S_{yy})\cos 2\theta}{2} \quad (19)$$

where S_{xx} and S_{yy} are the major and minor horizontal stress components and S_{xy} is a shear component that arises for an inclined well with respect to the in-situ stress tensor. Far-field displacements are negligible and. boundary conditions on T and p are obtained from the borehole and formation conditions.

To specify the PT system, it is convenient to define the following matrices M and C, and the vectors **b** and **V**:

$$M = \begin{bmatrix} \Psi & \Gamma \\ T_F\Gamma & T_F\Lambda \end{bmatrix},\ C = \begin{bmatrix} (k/\eta) & -K^T \\ -T_F K^T & k^T \end{bmatrix} \quad (20)$$

$$\mathbf{b} = \begin{bmatrix} \alpha \\ T_F A \end{bmatrix} \text{ and } \mathbf{V} = \begin{bmatrix} p \\ T \end{bmatrix} \quad (21)$$

Boundary conditions in two dimensions are given by:

$$\mathbf{V}(R_B, \theta, t) = \mathbf{V}_B(t) \text{ and } \mathbf{V}(R_F, \theta, t) = \mathbf{V}_F \quad (22)$$

and the initial condition is:

$$\mathbf{V}(r, \theta, 0) = \mathbf{V}_F \quad (23)$$

The PT system is then given as:

$$\sum_{i=1}^{2} M_{1j}\dot{V}_j - \nabla\cdot\sum_{i=1}^{2} C_{1j}\nabla V_j = -b_1\left(\nabla\cdot\dot{\mathbf{u}}\right) \quad (24)$$

$$\sum_{i=1}^{2} M_{2j}\dot{V}_j - \nabla\cdot\sum_{i=1}^{2} C_{2j}\nabla V_j = -b_2\left(\nabla\cdot\dot{\mathbf{u}}\right) \quad (25)$$

which are equivalent to the fully coupled fluid and thermal diffusion equations (14) and (15), respectively. The thermoporoelastic system may be solved using an approximation such that functions u, v, V_1, and V_2 are expanded as:

$$f(r, \theta) = f_0(r) + f_1(r)sin(2\theta) + f_2(r)cos(2\theta) \quad (26)$$

Numerical approximations of functions of r are obtained by approximating with `hat' functions in r defined over a uniform mesh with N_r equal subintervals on [R_B ,R_F]. The functions V_1 and V_2 are transformed to homogeneous Dirichlet boundary conditions that are imposed on the approximating functions. Imposed conditions are not required for displacements u and v since stress boundary conditions are related to Neumann boundary conditions. Time stepping in the diffusion system is carried out using a backward time-stepping method. The coefficients C_{ij} for i, j = 1, 2 are approximated with indicator I_k functions. The interval [0, 2π) is partitioned into N_θ equal sub-intervals. The annular domain

$$\Omega = \{(r, \theta) : R_B < r < R_F\ ,\ 0 \le \theta < 2\pi\} \quad (27)$$

is then partitioned into subsets Ω_k, k = 1,..., N = Nr x N_θ that are obtained as Cartesian products of subintervals from the [R_B ,R_F] partition and the [0,2π) partitions. The indicator functions are then defined by

$$I_k(r, \theta) = 1, \text{ if } (r, \theta) \text{ is in } \Omega_k, \text{ and 0 otherwise} \quad (28)$$

A coefficient is then expressed by a sum of the I_k functions. For example, we have

$$C_{ij} = \sum_{k=1}^{N} \tilde{C}_{ij} I_k(r, \theta) \quad (29)$$

where the coefficients $\tilde{C}_{ij}$ express the diffusion properties within the subset Ω_k.

RESULTS

General

This paper describes investigating and optimizing the temperature difference, ΔT, between a borehole and the surrounding formation to enhance the preconditioning of a particular well. Preconditioning can imply lowering of breakdown pressures, wellbore strengthening, modification of the initiation pattern of subsequent hydraulically generated fractures, etc. The developed model was used to analyze the problem of a fractured borehole subjected to non-hydrostatic in-situ stress fields.

Figure 2 shows the geometry around the perimeter of the borehole. The cyan filled circle represents the borehole. R_F is the outer radius of the region around the borehole where the temperature T_F (140 ^{o}C), pore pressure p_F (15.24 MPa), and stresses (σ_{xx} = 28.45 MPa, σ_{yy} = 21 MPa) are unaffected or equal to the original values in the formation. In this analysis, R_F = 20 R, where R is the borehole radius. The trace or center of the bi-wing healed fracture is represented by the dashed red line located at an angle γ from the x-axis. The half angular aperture of the fracture is expressed by $\delta\gamma = 0.25^o$ which is the angle between the fracture center (dashed red line) and fracture

boundary (solid red line). The permeability in the healed fracture (the annular section with an angle of $2\delta\gamma$ bounded by the two solid red lines) is 1000 times larger than that of the formation. Tables 1 and 2 summarize the properties and input parameters considered in this study.

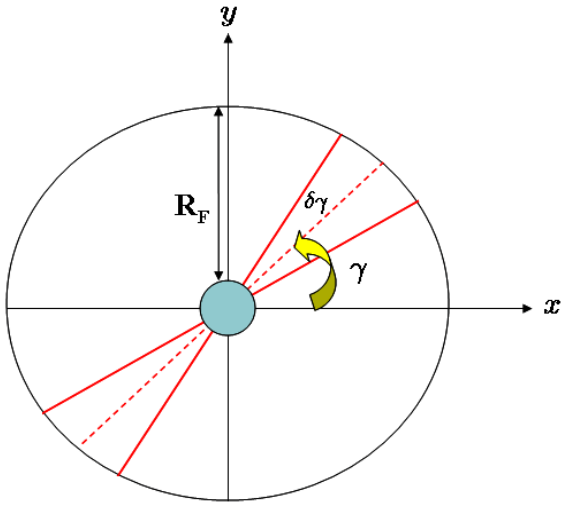

Figure 2: Geometry around the perimeter of the borehole (not to scale).

Table 1: Physical properties of rock/fluid system.

Drained Elastic modulus, E	56×10^9 Pa
Solid bulk modulus, K_s	37×10^9 Pa
Drained Poisson's Ratio, ν	0.15
Reference Porosity, ϕ	0.012
Fluid density, ρ_f	936 kg/m^3
Fluid specific heat capacity, C_f	4200 J/kg.^{o}K
Fluid bulk modulus K_f	2.28×10^9 Pa
Fluid volumetric thermal expansion coefficient, β_f	6.5×10^{-4} ^{o}C^{-1}
Solid density, ρ_s	2.65×10^3 kg/m^3
Solid specific heat capacity, C_s	900 J/kg.^{o}K
Solid volumetric thermal expansion coefficient, β_s	1.65×10^{-5} ^{o}C^{-1}
Permeability/fluid viscosity ratio k/η of formation k/η of healed fracture region	10^{-17} m^2/Pa.s 10^{-14} m^2/Pa.s
Rock (solid+fluid) thermal conductivity coefficient, k^T	4 W/m.^{o}K
Thermal osmosis coefficient, K^T	10^{-11} m^2/s.^{o}K

Table 2: Input parameters.

Time (after thermal pre-conditioning starts)	1/6, 1, 6, 12, 24, 72, 120 Hours
In situ stresses	σ_{xx} = 28.45 MPa σ_{yy} = 21.00 MPa
Formation pore pressure, p_F	15.24 MPa
Borehole pressure, p_B	26, 29, 32 MPa
Formation temperature, T_F	140 ^{o}C
Borehole temperature, T_B	80, 100, 120^{o}C
Wellbore radius, R	0.125 m

Effect of cooling on pore pressure and stresses

Figures 3-7 show the results for temperature differences ΔT = -20, -40, and -60^{o}C, the observed orientation at an angle of θ = 90^o (parallel to σ_{yy}) around the borehole perimeter, where the trace orientation of the healed fracture is at γ = 45^o, a borehole pressure p_B = 26 MPa, and after 1 and 120 hours of starting the thermal preconditioning.

It is shown that the cooler the borehole, the lower the pore pressure, and the more compressive or positive the effective radial stress is after a short time (e.g. 1 hr) and the less tensile or negative after a long time (e.g. 5 days) near the borehole. After a short time, the effective radial stress increases from zero at the wall (becomes more compressive) reaching a maximum value in the formation, before tending towards the far field stresses. However, after a long time, the effective radial stress decreases from zero at the wall (becomes more tensile) reaching a maximum negative value in the formation, before rising towards the far field stresses.

On the other hand, as cooling increases from ΔT = -20 to -60^{o}C, the effective tangential stress becomes more tensile or less compressive at the wall and in the formation. At the borehole wall, the effective tangential stress is lowest (most tensile) for the most negative value of ΔT (-60^{o}C). From the borehole wall (r = 0) to the far field ($r = R_F$), the effective tangential stress increases, becomes less tensile, changes sign, and reaches a maximum compressive (positive) value in the formation, before tending towards the far field stresses. The maximum tensile (most negative) effective tangential stress always occurs at the borehole wall while the maximum tensile effective radial stress always occurs in the formation.

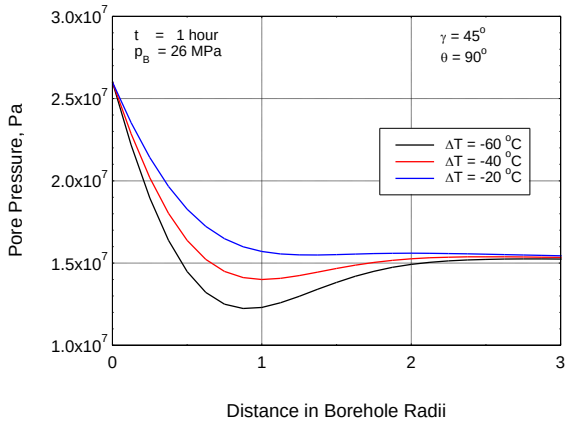

Figure 3: Pore pressure distributions for different cooling temperatures, angles θ = 90^o, γ = 45^o, borehole pressure p_B = 26 MPa, after 1hour.

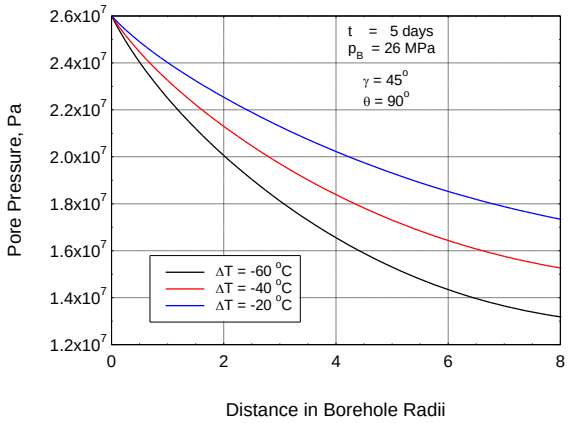

Figure 4: Pore pressure distributions for different cooling temperatures, angles $\theta = 90^o$, $\gamma = 45^o$, borehole pressure $p_B = 26$ MPa, after 5 days.

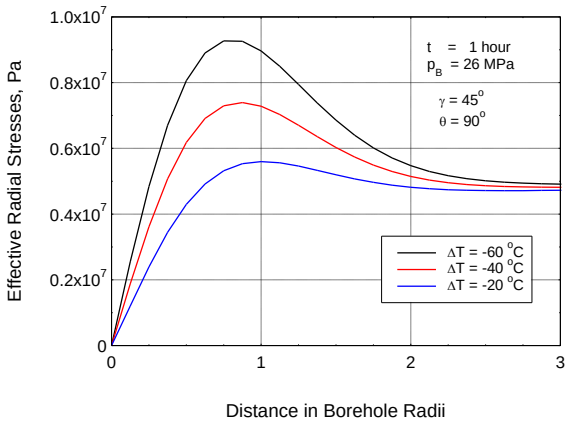

Figure 5: Effective radial stress distributions for different cooling temperatures, angles $\theta = 90^o$, $\gamma = 45^o$, borehole pressure $p_B = 26$ MPa, after 1 hour.

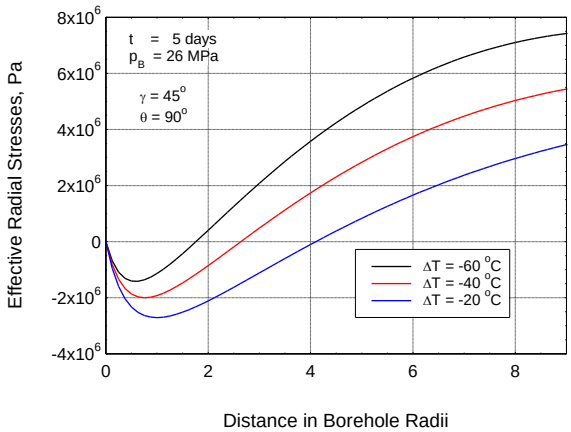

Figure 6: Effective radial stress distributions for different cooling temperatures, angles $\theta = 90^o$, $\gamma = 45^o$, borehole pressure $p_B = 26$ MPa, after 5 days.

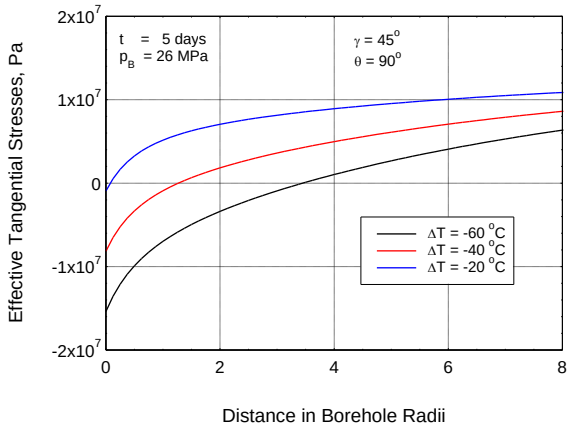

Figure 7: Effective tangential stress distributions for different cooling temperatures, angles $\theta = 90^o$, $\gamma = 45^o$, borehole pressure $p_B = 26$ MPa, after 5 days.

Effect of borehole pressure on stresses

Figures 8-10 show the results for different borehole pressure [p_B = 26 MPa (blue), 29 MPa (red), and 32 MPa (black)], a temperature difference ΔT = -40 °C, the observed orientation at an angle of θ = 90° (parallel to σ_{yy}) around the borehole perimeter, where the trace orientation of the healed fracture is at γ = 45°, and after 1 and 120 hours (5 days) of starting the thermal preconditioning.

Increasing the borehole pressure, p_B, decreases the compressive behavior and increases the tensile behavior of the effective radial stresses around the borehole. After a short time and for low p_B, the effective radial stress increases from zero (becomes positive or compressive), reaching a compressive maximum before descending towards the far field value. After a long time and/or for high p_B, the effective radial stress decreases below zero (becomes negative or tensile) reaching a tensile (negative) maximum before rising towards the far-field value. The maximum compressive or tensile effective radial stress always occurs in the formation near the borehole wall. The higher the borehole pressure, the higher (more negative) is the maximum tensile effective radial stress in the formation. The tensile effective radial stress could cause time-delayed spalling. Moreover, as the borehole pressure, p_B, increases, the effective tangential stress becomes more tensile at the borehole wall while more compressive farther away in the formation. The effective tangential stress increases from a negative value on the borehole wall (becomes less tensile or more compressive) reaching a maximum compressive value in the formation, before tending towards the far field stresses. The higher the borehole pressure, the more tensile is the effective tangential stress at and near the borehole wall, but more compressive farther away in the formation.

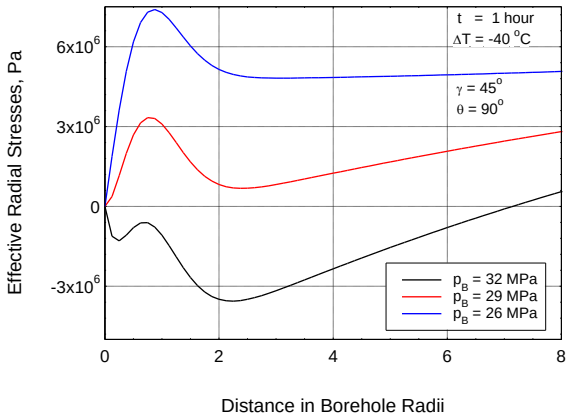

Figure 8: Effective radial stress distributions for different borehole pressures, angles θ = 90°, γ = 45°, ΔT = -40 °C, after 1 hour.

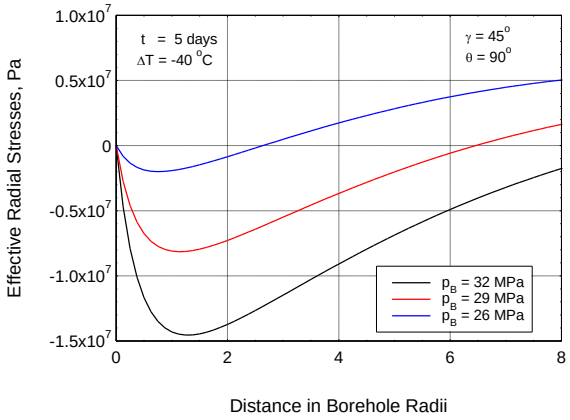

Figure 9: Effective radial stress distributions for different borehole pressures, angles θ = 90°, γ = 45°, ΔT = -40°C, after 5 days.

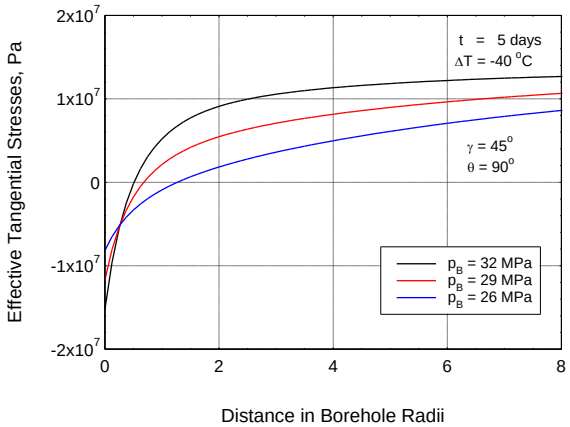

Figure 10: Effective tangential stress distributions for different borehole pressures, angles θ = 90°, γ = 45°, ΔT = -40°C, after 5 days.

Effect of time on pore pressure and stresses

Figures 11-17 show the results for a temperature difference of ΔT = -40°C, observed orientations at angles of θ = 0° (parallel to σ_{xx}), and 45° in the direction of the healed fracture trace (γ = 45°), a borehole pressure p_B = 29 MPa, and after 1/6 (blue), 1 (green), 6 (red), 12 (cyan), 24 (magenta), and 72 (yellow) hours of starting the thermal pre-conditioning.

For observed orientations far from the healed fracture trace (γ = 45°), at angles of θ = 0° (parallel to σ_{xx}) and 90° (parallel to σ_{yy}), the pore pressure decreases reaching a minimum value in the formation below the original formation pore pressure p_F. The pore pressure change decreases and moves away in the formation with time (Fig. 12). For observed orientations at or near the healed fracture trace (γ = 45°), at angles of θ = 45° or 30° and 60°, the pore pressure decreases to the far field value but remains above the original formation pore pressure p_F until the far field is reached at r = 20R (Fig. 13). After a short time and at angles of θ = 0° and 90°, the effective radial stress increases reaching a compressive peak that moves away in the formation with time (Fig.14). For observed orientations at or near the healed fracture trace (γ = 45°), the compressive (positive) maximum (except for very short durations, i.e. t = 10 min) is replaced by a tensile (negative) maximum (Fig. 15). After a long time, the effective radial stress becomes tensile (negative) near the wall before rising to the compressive far field value in the formation. The maximum tensile (most negative) effective radial stress occurs in the formation. The longer the time, the more tensile is this maximum. Note that cooling decreases the maximum tensile value in the formation near the wall. The tensile effective radial stress could cause time-delayed spalling within the formation. The changes of the effective tangential stresses near the wellbore wall are large after a short time; however, they decrease with time and move farther in the formation (Figs. 16-17). The maximum tensile effective tangential stress always occurs on the borehole wall.

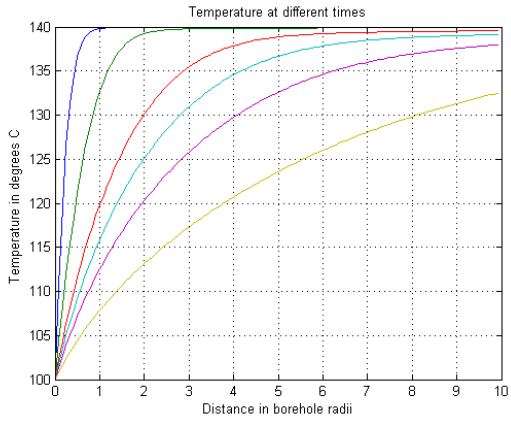

Figure 11: Temperature distributions after 1/6 (blue), 1 (green), 6 (red), 12 (cyan), 24 (magenta), and 72 (yellow) hours, for ΔT = -40°C.

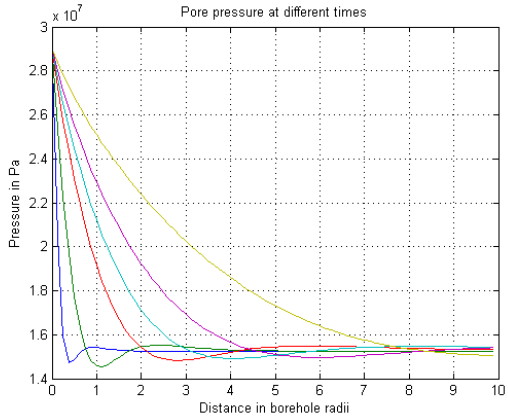

Figure 12: Pore Pressure distributions after 1/6 (blue), 1 (green), 6 (red), 12 (cyan), 24 (magenta), and 72 (yellow) hours, for ΔT = -40°C, p_B = 29 MPa, γ =45°, θ = 0°.

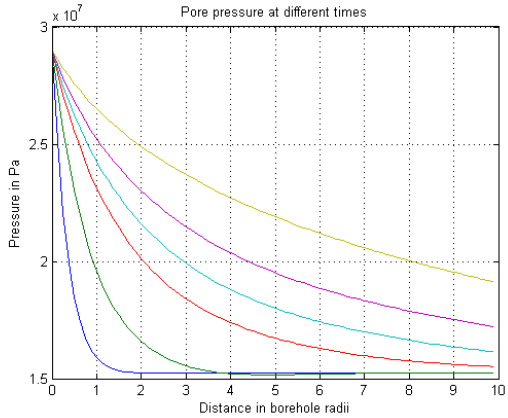

Figure 13: Pore Pressure distributions after 1/6 (blue), 1 (green), 6 (red), 12 (cyan), 24 (magenta), and 72 (yellow) hours, for ΔT = -40°C, p_B = 29 MPa, γ =45°, θ = 45°.

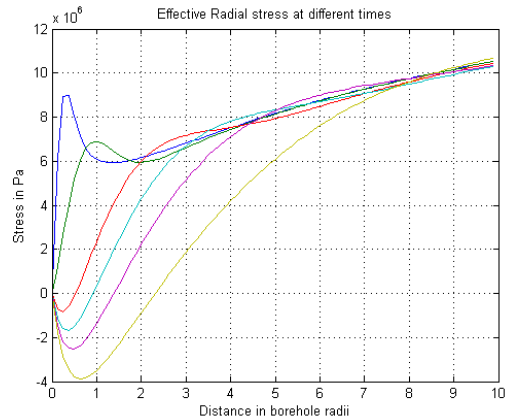

Figure 14: Effective radial stress distributions after 1/6 (blue), 1 (green), 6 (red), 12 (cyan), 24 (magenta), and 72 (yellow) hours, for ΔT = -40°C, p_B = 29 MPa, γ =45°, θ = 0°.

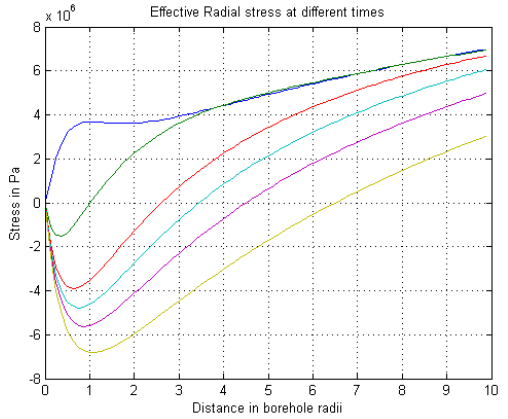

Figure 15: Effective radial stress distributions after 1/6 (blue), 1 (green), 6 (red), 12 (cyan), 24 (magenta), and 72 (yellow) hours, for ΔT = -40°C, p_B = 29 Mpa, θ = 45°.

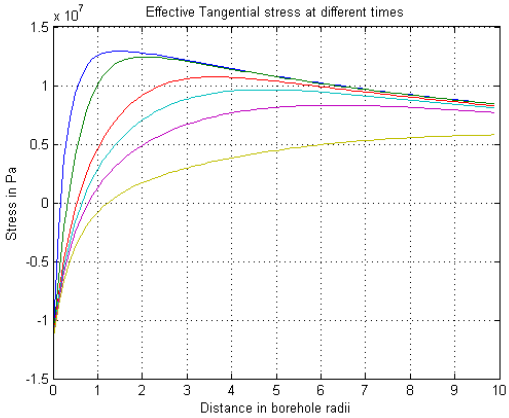

Figure 16: Effective tangential stress distributions after 1/6 (blue), 1 (green), 6 (red), 12 (cyan), 24 (magenta), and 72 (yellow) hours, for ΔT = -40°C, p_B = 29 MPa, γ =45°, θ = 0°.

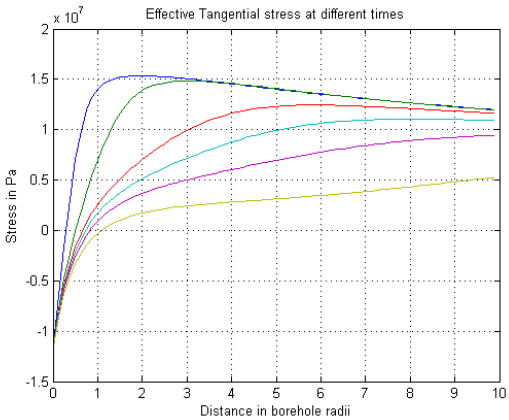

Figure 17: Effective tangential stress distributions after 1/6 (blue), 1 (green), 6 (red), 12 (cyan), 24 (magenta), and 72 (yellow) hours, for ΔT = -40°C, p_B = 29 MPa, γ =45°, θ = 45°.

Effect of angle θ on pore pressure and stresses

Figures 18-25 show the results for angles of θ = 0 (blue), 30 (green), 45 (red), 60 (cyan), and 90^o (magenta), around the borehole perimeter, where the trace orientation of the healed fracture is at $\gamma = 45^o$, a temperature difference ΔT = -40 ^{o}C, a borehole pressure p_B = 29 MPa, and after 1 and 6 hours of starting the thermal preconditioning. Note that the in situ stresses $\sigma_{xx} > \sigma_{yy}$. The behavior of the curves is better understood by dividing the curves into two sets. Set I: the set of orientations far from the healed fracture trace ($\gamma = 45^o$), at angles of $\theta = 0^o$ (blue) and 90^o (magenta); and Set II: the set of orientations at or near the healed fracture trace ($\gamma = 45^o$), at angles of θ = 30^o (green), 45^o (red), and 60^o (cyan). For set I, the decrease of the pore pressure is large near the borehole wall reaching a minimum below the formation pore pressure p_F. Note that the blue and magenta (θ = 0^o and 90^o) curves coincide. For set II, the decrease of the pore pressure remains above the formation pore pressure p_F near the borehole wall. However, the decrease is smallest in the direction of the healed fracture at $\theta = \gamma = 45^o$. Note that the green and cyan (θ = 30^o and 60^o) curves coincide. After a short time, the effective radial stress starting from zero at the wall becomes more compressive (positive) in the formation, reaching a maximum, before tending towards the far-field value. Note that the effective radial stress is highest in the σ_{xx}-direction (θ = 0^o). After a long time, the effective radial stress starting from zero at the wall becomes more tensile (negative) near the wall, reaching a negative maximum in the formation, before rising up towards the positive compressive far-field value. The highest negative maximum for set II occurs in the direction of θ = 60^o; whereas for set I, it occurs at θ = 90^o. Within each set, the higher the angle θ, the higher the compressive effective tangential stress is in the formation. The maximum tensile (most negative) effective tangential stress occurs at the borehole wall.

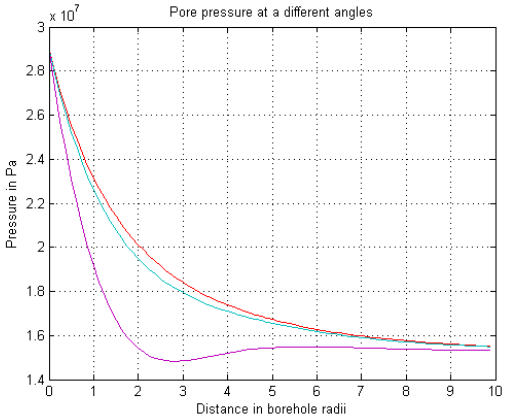

Figure 18: Pore pressure distribution for ΔT = -40 ^{o}C, p_B = 29 MPa, γ =45^o, at angles θ = 0 (blue), 30 (green), 45 (red), 60 (cyan), 90^o (magenta), after t = 6 hours.

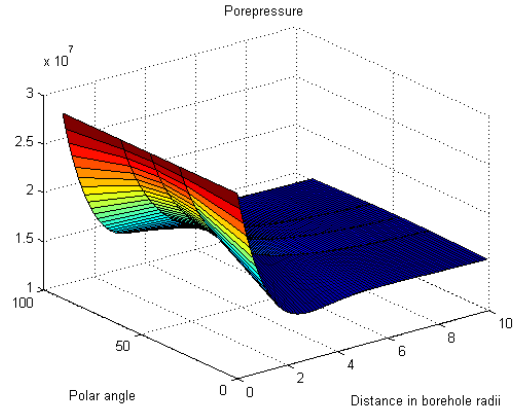

Figure 19: Pore pressure 3D distribution over distance and angles θ for ΔT = -40 ^{o}C, p_B = 29 MPa, γ =45^o, after t = 6 hours.

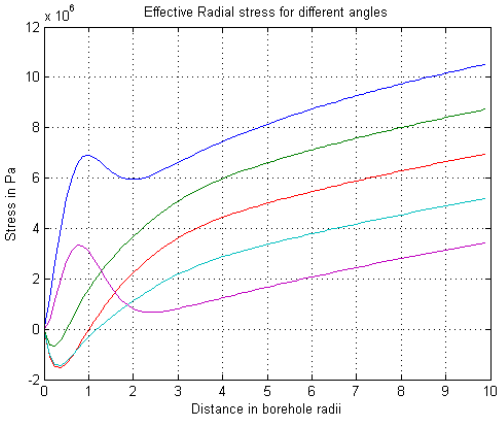

Figure 20: Effective radial stress distribution for ΔT = -40^{o}C, p_B = 29 MPa, γ =45^o, at angles θ = 0 (blue), 30 (green), 45 (red), 60 (cyan), 90^o (magenta), after t = 1 hour.

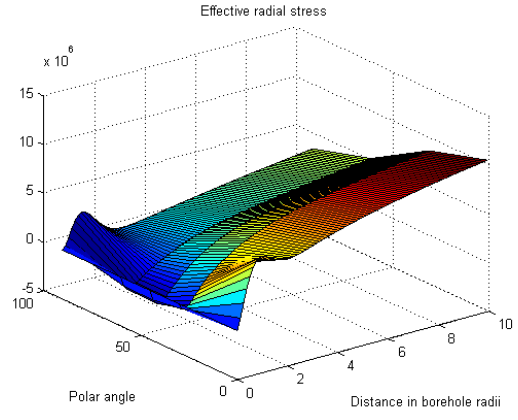

Figure 21: Effective radial stress 3D distribution over distance and angles θ for ΔT = -40 ^{o}C, p_B = 29 MPa, after t = 1 hour.

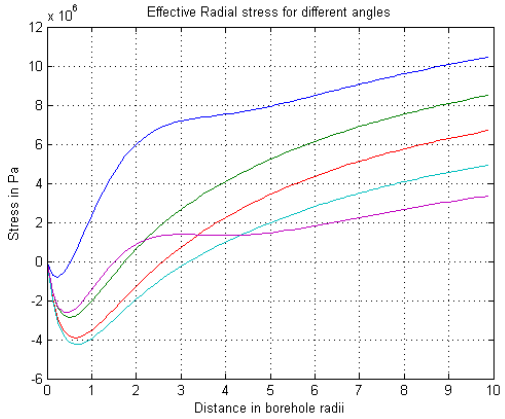

Figure 22: Effective radial stress distribution for ΔT = -40^{o}C, p_B = 29 MPa, γ =45^o, at angles θ = 0 (blue), 30 (green), 45 (red), 60 (cyan), 90^o (magenta), after t = 6 hours.

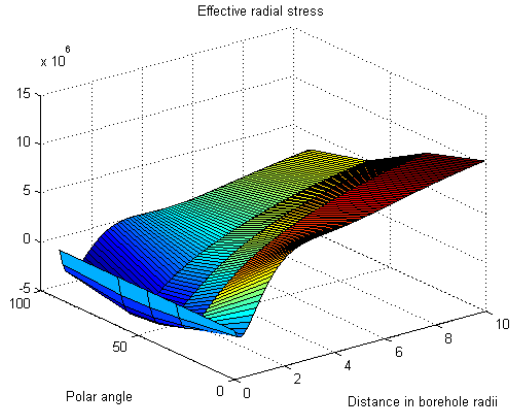

Figure 23: Effective radial stress 3D distribution over distance and angles θ for ΔT = -40 ^{o}C, p_B = 29 MPa, after t = 6 hours.

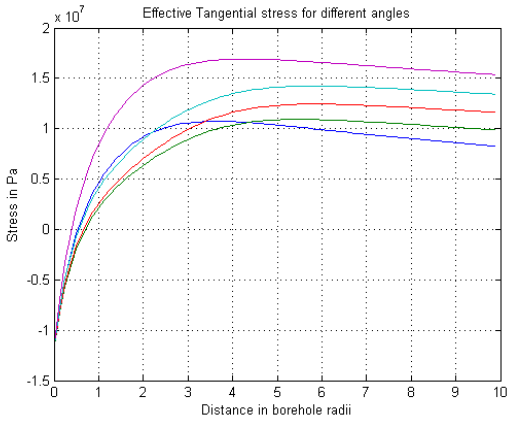

Figure 24: Effective tangential stress distribution for ΔT = -40 ^{o}C, p_B = 29 MPa, at angles θ = 0 (blue), 30 (green), 45 (red), 60 (cyan), 90^o (magenta), after t = 6 hours.

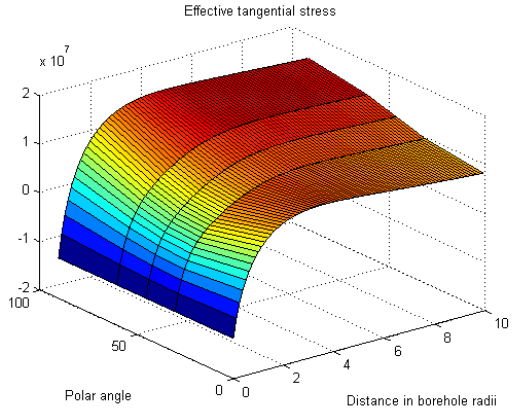

Figure 25: Effective tangential stress 3D distribution over distance and angles θ for ΔT = -40 ^{o}C, p_B = 29 MPa, after t = 6 hours.

CONCLUSIONS

The pore pressure and effective stresses around the fractured borehole are influenced by the temperature difference between the borehole and the formation (ΔT), the time (t), the borehole pressure (p_B), and the angle (θ) around the borehole perimeter. For example, the decrease of (1) the borehole temperature, or (2) the borehole pressure, or (3) the time results in higher (more compressive or less tensile) effective radial stresses and lower (less compressive or more tensile) effective tangential stresses around the wellbore. For Raft River well RRG-9, the maximum effective tangential tensile stress always occurs at the borehole wall while the maximum effective radial tensile stress always occurs in the formation. The tensile effective tangential stress could start the fracture at the wall and the tensile effective radial stress could cause time-delayed spalling. For observed orientations far from the healed fracture trace (γ = 45^o), at angles of θ = 0^o (parallel to σ_{xx}) and 90^o (parallel to σ_{yy}), the pore pressure decreases with cooling reaching a minimum value in the formation below the original formation pore pressure p_F. The pore pressure change increases with cooling but decreases and moves away into the formation with time. For observed orientations at or near the healed fracture trace (γ = 45^o), at angles of θ = 45^o or 30^o and 60^o, the pore pressure remains above the original formation pore pressure p_F until the far field is reached at r = 20R. After a short time and for observed orientations far from the healed fracture trace (γ = 45^o), at angles of θ = 0^o (parallel to σ_{xx}) and 90^o (parallel to σ_{yy}), the effective radial stress increases reaching a compressive peak that moves away into the formation with time. For observed orientations at or near the healed fracture trace (γ = 45^o), at angles of θ = 45^o or 30^o and 60^o the compressive maximum (except for very short durations, i.e. t = 10 min) is replaced by a tensile (negative) maximum. After a long time, the effective

radial stress becomes tensile (negative) near the wall before rising to the compressive far field value in the formation. The changes of the effective tangential stresses near the wellbore wall are large after a short time; however, they decrease with time and moves farther away in the formation.

For the conditions at Raft River well RRG-9, we recommend cooling the borehole by at least 40^{o}C to optimize the preconditioning of the well. At the present time, we are investigating the effect of ΔT on the shear stresses and the possibility of microcrack generation and reactivation of existing fractures. A three-dimensional model will then be developed.

ACKNOWLEDGMENTS

The authors thank the financial support by DOE under contract number DE-EE0000215 as well as the partial support by the Geothermal Program of Sandia National Laboratories.

REFERENCES

Ayling, B., Molling, P., Nye, R. and Moore, J. (2011), "Fluid geochemistry at the Raft River geothermal field, Idaho: new data and hydrogeological implications," Proceedings, 36th Workshop on Geothermal Reservoir Engineering Stanford University, Stanford, California, January 31 - February 2, 2011, SGP-TR-191.

Covington, H.R. (1980), "Subsurface geology of the Raft River geothermal field, Idaho," *GRC Transactions*, **4**, 113-115.

Diek, A., White, L. and Roegiers, J.-C. (2011), "A fully coupled thermoporoelastic model for drilling in HPHT formations," 12th International Congress on Rock Mechanics in Beijing, ISRM-2011; paper #184.

Diek, A., White, L. and Roegiers, J.-C. (2011), "A fully coupled thermoporoelastic model for drilling in chemically active formations," 45th US Rock Mechanics/Geomechanics Symposium in San Francisco, CA, June 26-29, ARMA-11, paper #406.

Diek, A., White, L. and Roegiers, J.-C. (2011), "A fully coupled thermoporoelastic model for drilling in geological formations," Geothermal Resources Council 35th Annual Meeting October 23-26, 2011 in San Diego, California, paper #176.

Onsager, L. (1931), "Reciprocal relations in irreversible processes I & II," *Physical Reviews,* **37,** 405-426; **38,** 2265-2279.

Mabey, D.R., Hoover, D.B., O'Donnell, J.E. and Wilson, C.W. (1978), "Reconnaissance geophysical studies of the geothermal systems in southern Raft River valley, Idaho," *Geophysics*, **43**(7), 1470-1484.